The ASTRODEEP Frontier Fields catalogues. I. Multiwavelength photometry of Abell-2744 and MACS-J0416

A&A 590, A30 (2016)
DOI: 10.1051/0004-6361/201527513

Astronomy & Astrophysics

The ASTRODEEP Frontier Fields catalogues

I. Multiwavelength photometry of Abell-2744 and MACS-J0416⋆

E. Merlin[1], R. Amorín[1], M. Castellano[1], A. Fontana[1], F. Buitrago[2,10,11], J. S. Dunlop[2], D. Elbaz[3], A. Boucaud[4,12], N. Bourne[2], K. Boutsia[1], G. Brammer[5], V. A. Bruce[2], P. Capak[6], N. Cappelluti[7], L. Ciesla[3], A. Comastri[7], F. Cullen[2], S. Derriere[8], S. M. Faber[9], H. C. Ferguson[5], E. Giallongo[1], A. Grazian[1], J. Lotz[5], M. J. Michałowski[2], D. Paris[1], L. Pentericci[1], S. Pilo[1], P. Santini[1], C. Schreiber[3,13], X. Shu[3,14], and T. Wang[3,15]

[1] INAF−Osservatorio Astronomico di Roma, via Frascati 33, 00078 Monte Porzio Catone (RM), Italy
e-mail: emiliano.merlin@oa-roma.inaf.it
[2] SUPA, Institute for Astronomy, University of Edinburgh, Royal Observatory, Edinburgh, EH9 3HJ, UK
[3] Laboratoire AIM-Paris-Saclay, CEA/DSM/Irfu − CNRS − Université Paris Diderot, CEA-Saclay, pt courrier 131, 91191 Gif-sur-Yvette, France
[4] IAS − Institut d'Astrophysique Spatiale, Université Paris Sud, Bâtiment 121, 91405 Orsay, France
[5] Space Telescope Science Institute, 3700 San Martin Drive, Baltimore, MD 21218, USA
[6] Spitzer Science Center, 314-6 Caltech, Pasadena, CA 91125, USA
[7] INAF−Osservatorio Astronomico di Bologna, via Ranzani 1, 40127 Bologna, Italy
[8] Observatoire astronomique de Strasbourg, Université de Strasbourg, CNRS, UMR 7550, 11 rue de l'Université, 67000 Strasbourg, France
[9] UCO/Lick Observatory, University of California, 1156 High Street, Santa Cruz, CA 95064, USA
[10] Instituto de Astrofísica e Ciências do Espaço, Universidade de Lisboa, OAL, Tapada da Ajuda, 1349-018 Lisbon, Portugal
[11] Departamento de Fisica, Faculdade de Ciências, Universidade de Lisboa, Edificio C8, Campo Grande, 1749-016 Lisbon, Portugal
[12] Sorbonne Universités, UPMC Univ. Paris 6 et CNRS, UMR 7095, Institut d'Astrophysique de Paris, 98bis Bd Arago, 75014 Paris, France
[13] Leiden Observatory, Leiden University, 2300 RA Leiden, The Netherlands
[14] Department of Physics, Anhui Normal University, Wuhu, 241000 Anhui, PR China
[15] School of Astronomy and Astrophysics, Nanjing University, 210093 Nanjing, PR China

Received 6 October 2015 / Accepted 13 March 2016

ABSTRACT

Context. The Frontier Fields survey is a pioneering observational program aimed at collecting photometric data, both from space (*Hubble* Space Telescope and *Spitzer* Space Telescope) and from ground-based facilities (VLT Hawk-I), for six deep fields pointing at clusters of galaxies and six nearby deep parallel fields, in a wide range of passbands. The analysis of these data is a natural outcome of the ASTRODEEP project, an EU collaboration aimed at developing methods and tools for extragalactic photometry and creating valuable public photometric catalogues.

Aims. We produce multiwavelength photometric catalogues (from B to 4.5 μm) for the first two of the Frontier Fields, Abell-2744 and MACS-J0416 (plus their parallel fields).

Methods. To detect faint sources even in the central regions of the clusters, we develop a robust and repeatable procedure that uses the public codes GALAPAGOS and GALFIT to model and remove most of the light contribution from both the brightest cluster members, and the intra-cluster light. We perform the detection on the processed HST $H160$ image to obtain a pure H-selected sample, which is the primary catalogue that we publish. We also add a sample of sources which are undetected in the $H160$ image but appear on a stacked infrared image. Photometry on the other HST bands is obtained using SEXTRACTOR, again on processed images after the procedure for foreground light removal. Photometry on the Hawk-I and IRAC bands is obtained using our PSF-matching deconfusion code T-PHOT. A similar procedure, but without the need for the foreground light removal, is adopted for the Parallel fields.

Results. The procedure of foreground light subtraction allows for the detection and the photometric measurements of ∼2500 sources per field. We deliver and release complete photometric H-detected catalogues, with the addition of the complementary sample of infrared-detected sources. All objects have multiwavelength coverage including B to H HST bands, plus K-band from Hawk-I, and 3.6−4.5 μm from *Spitzer*. full and detailed treatment of photometric errors is included. We perform basic sanity checks on the reliability of our results.

Conclusions. The multiwavelength photometric catalogues are available publicly and are ready to be used for scientific purposes. Our procedures allows for the detection of outshone objects near the bright galaxies, which, coupled with the magnification effect of the clusters, can reveal extremely faint high redshift sources. Full analysis on photometric redshifts is presented in Paper II.

Key words. catalogs – methods: data analysis – galaxies: photometry – galaxies: high-redshift

⋆ The catalogues, together with the final processed images for all HST bands (as well as some diagnostic data and images), are publicly available and can be downloaded from the Astrodeep website at http://www.astrodeep.eu/frontier-fields/ and from a dedicated CDS webpage (http://astrodeep.u-strasbg.fr/ff/index.html). The catalogues are also available at the CDS via anonymous ftp to cdsarc.u-strasbg.fr (130.79.128.5) or via http://cdsarc.u-strasbg.fr/viz-bin/qcat?J/A+A/590/A31

1. Introduction

Multiwavelength photometric catalogues are a fundamental tool for investigating the properties of high-redshift galaxies, where large statistical spectroscopic studies are unfeasible and morphology is unclear. With the aid of the most powerful telescopes available, such as the *Hubble* Space Telescope (HST), the *Spitzer* Space Telescope, and ground based facilities, such as the Large Binocular Telescope and the Very Large Telescope (VLT), it has become possible to build large libraries of photometric data on the faintest and most distant sources in selected regions of the sky (see, e.g. Guo et al. 2013; Agüeros et al. 2005; Obrić et al. 2006; Grogin et al. 2011).

The Frontier Fields (FF) progam (Lotz et al. 2014; Koekemoer et al. 2014) offers a unique opportunity to obtain high quality data of unprecedented depth. Thanks to the natural magnification provided by the foreground galaxy clusters that were targeted by the observations, it is possible to observe extremely faint galaxies, which have been enhanced in luminosity by the gravitational lensing provided by the clusters' mass. The vast scale of the program (six cluster fields plus six parallel fields) also reduces cosmic variance effects in the analysis of data from previous surveys. Moreover, the program offers a crucial test for our current capabilities of data analysis, from the perspective of the new, large amount of data that will come from future facilities like the *James Webb* Space Telescope. Published works on FF data include McLeod et al. (2015), Wang et al. (2015), Oesch et al. (2015), Laporte et al. (2015), Atek et al. (2015).

However, the conceptual and technical challenges in the analysis of these data are huge. Combining all the available data at different wavelengths and resolution is in itself an extremely difficult task. On top of that, the presence of bright cluster members and the intra-cluster light (ICL) make the whole procedure more complicated: they cover a significant fraction of the highly magnified region, outshining the faintest sources and making the whole background variable and difficult to estimate.

A possible way to fully exploit the depth of the observations that we explore in this paper is to try to "remove" these objects artificially from the field of view, via analytic fitting. We present a complete multiwavelength photometric catalogue for the first two observed FF, Abell-2744 (A2744 hereafter) and MACS-J0416 (M0416 hereafter) (two cluster fields plus two parallel fields), along with a detailed description of the methodology we have developed to obtain these photometric data. The catalogues were obtained using techinques and software developed within the ASTRODEEP project[1]. The detection was performed on the HST $H160$ image. We also add an additional set of sources detected in a stacked infrared (HST $Y + J + JH + H$) image, to recover additional faint sources. The final photometric catalogue consists of ten bandpasses: HST ACS $B435$, $V606$, $I814$; HST WFC3 $Y105$, $J125$, $JH140$ and $H160$; VLT Hawk-I Ks 2.146 μm (ground based), and *Spitzer* IRAC 3.6 and 4.5 μm.

To detect and measure the fluxes from the faint sources hidden behind the extended halos of the bright cluster galaxies and within the ICL, we developed an articulate procedure to process the two cluster images with the goal of removing the foreground light, letting the fainter and hidden sources behind it appear. The parallel fields, on the other hand, did not require this kind of intervention and could be processed straightforwardly with the same approach used in the CANDELS campaign (see Galametz et al. 2013, for a description of the adopted methods).

The final catalogues and images are publicly available and can be downloaded from the ASTRODEEP website[2]; images and catalogues can also be browsed from a dedicated CDS interface[3]. A companion paper (Castellano et al. 2016, C16 hereafter) presents the first scientific applications (photometric redshifts, magnification, and physical properties). Throughout these works, AB magnitudes have been adopted.

The structure of this paper is as follows: Sect. 2 describes the dataset we use in this study. Section 3 gives a detailed description of the procedure we applied to remove foreground light from the cluster detection $H160$ image. In Sect. 4, we describe how the detection catalogue is produced, and in Sect. 5 the recipes used to obtain photometric measurements on the other HST bands are presented. Section 6 presents the method we adopted to obtain the photometric measurements on the Ks and IRAC bandpasses. Section 7 describes an additional and complementary detection process that we perform on a stack of four infrared images. Section 8 presents diagnostics on the reliability of the results. Finally, Sect. 9 provides a summary of the work and a discussion of the results, and a description of the released catalogues is provided in the Appendix.

2. The dataset

A2744 and M0416 image datasets are the first two publicly released out of a total of six twin fields, observed by HST in parallel (i.e. the cluster pointing together with a "blank" parallel pointing) over two epochs, to a final depth of 140 orbits per field (FF program 13495, P.I. Lotz). The A2744 dataset also includes data acquired under programs 11689 (P.I. Dupke), 11386 (P.I. Rodney), and 13389 (P.I. Siana). The M0416 dataset combines the FF program data with imaging from the CLASH survey (P.I. Postman) and program 13386 (P. I. Rodney). The HST dataset consists of the following three optical and four near-infrared bands: $B435$, $V606$ and $I814W$ (ACS); $Y105$, $J125$, $JH140$, and $H160$ (WFC3). We use the final reduced and calibrated v1.0 mosaics released by STScI, drizzled at 0.06″ pixel-scale. A detailed description of the acquisition strategy and of the data-reduction pipeline, as well as the final number of orbits in each band, can be found in the STScI data release documentation[4].

Additional information redward of WFC3 $H160$ band is a fundamental ingredient for selecting and investigating extragalactic sources across a wide redshift range. We use the publicly released Hawk-I Ks images of the A2744 and M0416 fields (P. I. Brammer, ESO Programme 092.A-0472[5]), resampled to the HST pixel scale using SWARP (Bertin et al. 2002). The final exposure time is 29.43 and 25.53 h for A2744 and M0416, respectively. Finally, we include IRAC 3.6 and 4.5 μm data, acquired under DD time and, in the case of M0416, Cycle-8 program iCLASH (80168, P.I. Capak). The final exposure time is ~50 h per field.

In Table 1 we list point spread function (PSF) FWHM and depths (see Sects. 5 and 6) of all the imaging data under investigation. To estimate the limiting magnitudes of Hawk-I and IRAC images, we use the rms maps, corrected as explained in Sect. 6.1. The resulting values are in good agreement with those obtained by Laporte et al. (2015).

[1] ASTRODEEP is a coordinated and comprehensive program of i) algorithm/software development and testing; ii) data reduction/release; and iii) scientific data validation/analysis of the deepest multiwavelength cosmic surveys. For more information, visit http://astrodeep.eu

[2] http://www.astrodeep.eu/frontier-fields/

[3] http://astrodeep.u-strasbg.fr/ff/index.html

[4] https://archive.stsci.edu/pub/hlsp/frontier/

[5] http://gbrammer.github.io/HAWKI-FF/

Table 1. PSF FWHM and depths of the dataset.

Image	PSF *FWHM* (″)	Limiting AB magnitude	PSF *FWHM* (″)	Limiting AB magnitude
	A2744 Cluster		A2744 Parallel	
ACS *B*435	0.11	28.58	0.12	28.97
ACS *V*606	0.11	28.71	0.15	29.06
ACS *I*814	0.13	29.03	0.13	29.17
WFC3 *Y*105	0.18	29.15	0.19	29.30
WFC3 *J*125	0.19	28.83	0.19	28.88
WFC3 *JH*140	0.19	28.93	0.20	28.91
WFC3 *H*160	0.20	29.11	0.20	29.06
Hawk-I *K*s 2.146	0.38	26.13	0.38	26.12
IRAC 3.6	1.66	24.83	1.66	24.83
IRAC 4.5	1.72	24.87	1.72	24.87
	M0416 Cluster		M0416 Parallel	
ACS *B*435	0.12	28.86	0.13	28.81
ACS *V*606	0.16	28.97	0.13	28.83
ACS *I*814	0.16	29.31	0.18	29.19
WFC3 *Y*105	0.18	29.22	0.18	29.28
WFC3 *J*125	0.19	28.90	0.18	29.05
WFC3 *JH*140	0.20	28.95	0.19	29.12
WFC3 *H*160	0.20	29.01	0.20	29.14
Hawk-I *K*s 2.146	0.38	26.18	0.38	26.26
IRAC 3.6	1.66	25.04	1.66	25.11
IRAC 4.5	1.72	25.05	1.72	24.89

Notes. Limiting magnitudes of HST images have been computed as the magnitudes within $2\times FWHM_{H160}$ (=0.2″) circular apertures of 5σ sources, measured with SExtractor on PSF-matched images. Hawk-I and IRAC limiting magnitudes have been obtained computing $f_{5\sigma} = 5\times\sqrt{A_{\rm aper}}\times f_{\rm rms}$ in each pixel and taking the mode of the distributions ($A_{\rm aper}$ is the area of a circular region with radius $r_{{\rm aper},Ks} = 0.4''$, $r_{\rm aper,IRAC1} = 1.66''$, $r_{\rm aper,IRAC2} = 1.72''$).

3. Preparing the cluster detection images

As anticipated, the goal of obtaining a deep and complete catalogue requires the development of a method to remove the light from foreground objects in the clusters fields. For this, the first step is performed on the image on which the detection of sources will be performed, i.e. the WFC3 *H*160 band. As described in detail later, we finally add a subset of sources detected on a different image (namely, a stack of infrared HST images), but the bulk of the detection is performed on the *H*-band, as in the CANDELS and 3D-HST surveys, with which we choose to keep consistency. We therefore focus our attention on the *H*-band detection process, leaving the description of the infrared stacking detection to Sect. 7.

Our basic strategy is to use the public code Galfit (Peng et al. 2010) to model as accurately as possible both the ICL and the brightest cluster members, and eventually subtract them from the images. We fine-tune our procedure by testing several possible variants. Experimenting multicomponent, multi-object fits with Galfit is a particularly tedious and time-consuming exercise, partly because of the large computing time required by Galfit, and mostly because of the numerical instabilities in its convergence. We have chosen to present the final solution that we adopted, that provided us with the best result in the object subtraction. As shown below, it involves an iterative fitting of ICL and bright galaxies, in separate steps. Unfortunately, the conceptually most appealing solution (i.e. a simultaneous fit of both ICL and bright galaxies) did not produce comparably good results because of the degeneracy of allowed mathematical solutions to the problem, and has not been adopted here.

The final product of the whole process is a residual image in which the ICL and the bright objects have been subtracted efficiently. It is important to stress that the goal of the procedure is not to obtain physically reasonable numbers for light profile slopes and magnitudes (although, in most cases, we do get sensible figures, which is, of course, reassuring, see Sect. 8 and Fig. 11), but only to clean the image in the most efficient way, allowing for a more effective detection of faint sources. To obtain the most accurate models would require a tailor-made, ad hoc fine-tuning by hand of all the parameters and constraints involved (as performed for example by Giallongo et al. 2014). However, this would be beyond our aims of simply improving the catalogue assembly, and it would not be repeatable on different fields without close supervision. Therefore, we choose to stick to our simpler approach.

The basic steps we perform to remove the light of the cluster sources are as follows:

- *STEP 1*: after masking the brightest galaxies of the cluster, we fit the diffuse ICL component using Galfit to obtain a first approximation model for the ICL, which we eventually subtract from the original image.
- *STEP 2*: on the ICL-subtracted image, we use the public code Galapagos (Barden et al. 2012) to obtain a first guess of the selected bright galaxies analytic profile.
- *STEP 3*: again on the ICL-subtracted image, we use Galfit to refine the first Galapagos fit, including multiple

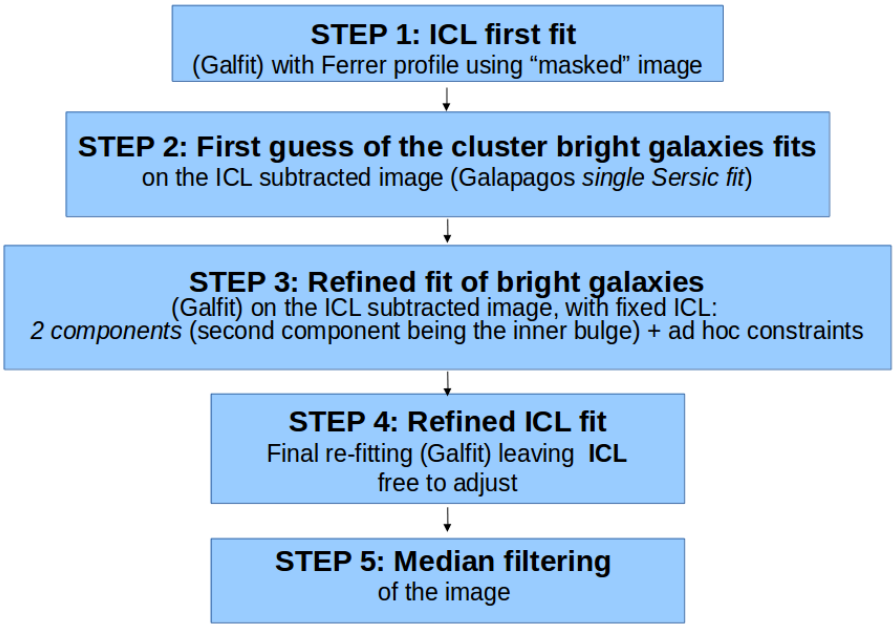

Fig. 1. Schematic description of the procedure applied to "clean" the cluster images, removing the light from the foreground bright sources.

components to better match the light profile in the central regions of the sources.

- *STEP 4*: on the original image we leave the ICL fit free to adjust, keeping the fits for the galaxies[6] frozen.
- *STEP 5*: we eventually apply a median filter on the residual images, which removes the remaining intermediate scale background residuals.

The global method is sketched in the flowchart in Fig. 1. Below, we describe in more detail each step of the procedure.

3.1. ICL first guess fit

To obtain a reasonable first guess model for the ICL, we first crudely mask out the contribution of the brightest sources. To do so, we start estimating the $1\sigma_{\rm sky}$ level of the H-band image by measuring σ in relatively small and blank boxes that are distributed homogeneously in regions sufficiently far from the cluster core; then we produce a mask image from the H-band image where all pixels above $8\sigma_{\rm sky}$ are excluded from the GALFIT fit. This cut masks out most of the light from the brightest sources in the core of the cluster, leaving enough pixels to fit the ICL with GALFIT.

To do so, we also need information on the image noise and the PSF. We let GALFIT create a noise image internally, using the `gain`, `exptime`, and `rdnoise` header parameters of the science image. On the other hand, we create a PSF model by stacking the cutouts of isolated, bright, but not saturated stars in the field, selected with an ad hoc SEXTRACTOR routine (we use version 2.8.6 in this work).

Then, following Giallongo et al. (2014), we use GALFIT (version 3.0.2) to fit a modified Ferrer profile (Binney & Tremaine 1987),

$$\Sigma = \Sigma_0\,(1-(r/r_{\rm out})^{2-\beta})^{\alpha} \qquad (1)$$

to the diffuse ICL distribution to all pixels with non-zero values. The Ferrer profile has an almost flat core and an outer truncation set by $r_{\rm out}$, being similar in shape to a Sérsic profile (Sérsic 1968) of index $n < 0.5$ (see next section). First guesses for Σ_0, $r_{\rm out}$, β, and α were estimated from the 1D isophotal profile.

The initial best-fit model for the ICL is intended to describe the overall shape of the ICL profile. For this reason, in addition to the Ferrer profile, we leave the position angle, the axis ratio, and the boxiness/diskyness parameter of the models free to vary. In addition, for A2744, we add one bending mode ($B2$) to follow the global shape of the ICL isophotes. For M0416, instead, we find our best fit using two Ferrer components, without bending modes.

3.2. Bright galaxies first guess fit

To fit the bright foreground galaxies that belong to the clusters, we follow an iterative procedure. GALFIT is a very powerful tool but can be prone to degeneracy instabilities when dealing with multicomponent fitting. To avoid the risk of misinterpreting local minima as best fits, we proceed with steps of increasing complexity, first fitting the objects with a single Sérsic profile,

$$\Sigma(R) = \Sigma_{\rm e}\exp\left\{-b_n\left[\left(\frac{r}{r_{\rm e}}\right)^{1/n_{\rm Sersic}}-1\right]\right\}, \qquad (2)$$

and then refining the fit, adding secondary components, as described in more details in the following sections.

The first step is performed by means of a GALAPAGOS run on the ICL-subtracted image. GALAPAGOS is a software package which directly links SEXTRACTOR and GALFIT, allowing for a smooth dataflow from the detection of sources to the estimation of their analytical fit. It is extremely useful for automatic and simultaneous fitting of many objects, also removing fainter contaminants, which are of course very numerous in our case.

To identify the bright objects we want to fit, we take advantage of the first stage of the GALAPAGOS pipeline, which consists of a SEXTRACTOR run to detect sources and measure the background. We select galaxies with `MAG_AUTO` < 19, retrieving 15 objects in the case of A2744, and 20 in the case of M0416.

[6] We emphasise that attempts to leave both the ICL and galaxies free to adjust in a final step gave unsatisfactory results because of the degeneracy of allowed mathematical solutions to the problem. Fitting the ICL alone proved to provide a cleaner result.

We then run the subsequent GALAPAGOS stages, automatically fitting the selected sources with single-Sérsic analytical profiles (the fit is performed including the neighbouring galaxies and the local background). For each object, we obtain an analytical model giving the best estimation of the total magnitude, the effective radius r_e, the Sérsic index $n_{\rm Srsic}$, the axis ratio, and the sky-projected position angle.

3.3. Bright galaxies refinement fit

We then proceed to the refinement stage, again on the ICL subtracted image, directly using GALFIT with the output parameters from the GALAPAGOS fits as a starting point. We introduce a second component to fit the central regions of the objects more accurately. In practice, we include a "bulgy" component, with $n_{\rm Sersic} > 4$ and axis ratio $q > 0.5$, alongside a generally more "disky" component, which we force to have $n_{\rm Sersic} < 4.5$ [7]. At this stage, all fitting parameters are left free to vary, with constraints on positions (±1 pixels for the disky component, ±3 for the bulgy component), magnitudes (±1 for the disky component, −1/+5 for the bulgy component), effective radii (1 to 60 pixels for the disky component, 1 to 30 for the bulgy component), Sérsic index (0.5 to 4.5 for the disky component, 4 to 8 for the bulgy component), and axis ratio (0.5 to 1 for the bulgy component).

When necessary, we further refine the fit with additional loops to add more components (for example, in the case of a very bright and centrally concentrated source in M0416, for which a PSF-shaped source has been added to the two main components).

3.4. ICL refinement fit

We finally run GALFIT again on the original, pre-ICL subtraction image, fixing all galaxy parameters and adding the ICL model(s). The ICL centroid position, the central surface brightness, and the truncation radius are left free to adjust (with constraints ±1 pixel, 25 to 27, and 1000 to 8000 pixels, respectively). Reassuringly, the final fit does not dramatically diverge from the first guess: the central surface brightness Σ_0 changes from 25.89 to 25.38 for A2744 and from 25.50 to 25.53 (first component) and from 25.50 to 25.84 (second component) for M0416. Radii and morphological shapes undergo similar minor changes as well.

3.5. Median filtering

The final step of our procedure aims at further improving the detection and the photometry in regions close to bright galaxy centres by mitigating the effects of small scale negative GALFIT residuals, which could hamper local background estimates. We use the IRAF task `median` to create a median-filtered version of the residual images over a $1'' \times 1''$ box. To avoid affecting low signal-to-noise pixels that belong to the detected sources, we exclude from the computation all pixels at $>1\sigma_{\rm SEx}$ above zero counts (where $\sigma_{\rm SEx}$ is computed by SEXTRACTOR), and their nearest neighbours. The resulting median-filtered image is then subtracted from the original one, obtaining a clear improvement in the innermost regions of the cluster. A comparison of the photometry extracted from the original residual image and the median-subtracted one shows no significant difference for any source far from the cluster centre, demonstrating that this last step is effective at improving the processed images while leaving flux measurements unaltered; this is further confirmed from simulation tests (see Sects. 4.2 and 5) showing that measured fluxes of test fake sources are less scattered with respect to their true input fluxes when performing measurements on the median-subtracted image. Figure 2 shows the effects of the procedure on the two cluster fields.

[7] Of course, a Sérsic index $n_{\rm Sersic} \sim 4$ can hardly describe a disk; here we use this terminology for the sake of conciseness.

Table 2. Total number of detected sources on the $H160$ images in the four considered fields.

Image	$N_{\rm detect}$	Image	$N_{\rm detect}$
$A2744_{\rm cl}$	2596 (+15)	$M0416_{\rm cl}$	2556 (+20)
$A2744_{\rm par}$	2325	$M0416_{\rm par}$	2581

Notes. The numbers in brackets are the models of bright cluster objects (15 for $A2744_{\rm cl}$, 20 for $M0416_{\rm cl}$).

3.6. Corrected root mean square (rms) map

As a final refining step, we use the GALFIT model image to estimate, on the basis of the image exposure time, the photon noise in each pixel contributed by the bright GALFIT-subtracted sources. The resulting photon-noise image is then added to the original rms map, to take into account the effect of the aforementioned subtracted sources on the detection and the flux measurement in the innermost cluster regions.

4. Obtaining the detection catalogues

4.1. Detection strategy

To obtain the final detection catalogues on the H-processed images, we use SEXTRACTOR with a `HOT+COLD` approach (Galametz et al. 2013). This procedure adopts two different sets of the SEXTRACTOR parameters to detect objects at different spatial scale. The COLD mode is used to detect bright extended sources with relatively low efficiency in deblending. The HOT mode is more efficient for faint galaxies and is used to detect small sources outside the region of the brightest sources that are already detected with the COLD mode. Typically, the COLD mode is used to detect sources that are 1.5 mag brighter than the detection limit. We note that, in both cases, we refer to objects that are fainter than the brighter cluster members that we have already fitted and removed. Considering that in the clusters fields, even after the described procedure helped to clean out the image, many faint sources lie within, or nearby, extended halos of bright galaxies, we find it more convenient to adopt a more aggressive set of parameters so that our `COLD` detection actually corresponds to the CANDELS `HOT` detection. Very faint sources are then detected using an even more extreme choice of parameters so that our `HOT` detection turns out to be "hotter" than the CANDELS one, with an aggressive choice for the background subtraction. We choose to use the same recipe on the parallel fields as well. We list the relevant parameters adopted in this procedure in the Appendix.

Table 2 lists the total number of detected sources on the $H160$ images in the four fields under consideration. It is interesting to check how much our procedure to remove ICL and bright cluster galaxies improves the detection of faint sources. For this purpose, we compare the number of detected sources in the A2744 cluster field with respect to a `HOT+COLD` SEXTRACTOR run on the original H-band image (using identical parameter settings for the detection). The results are shown in Figs. 3 and 4.

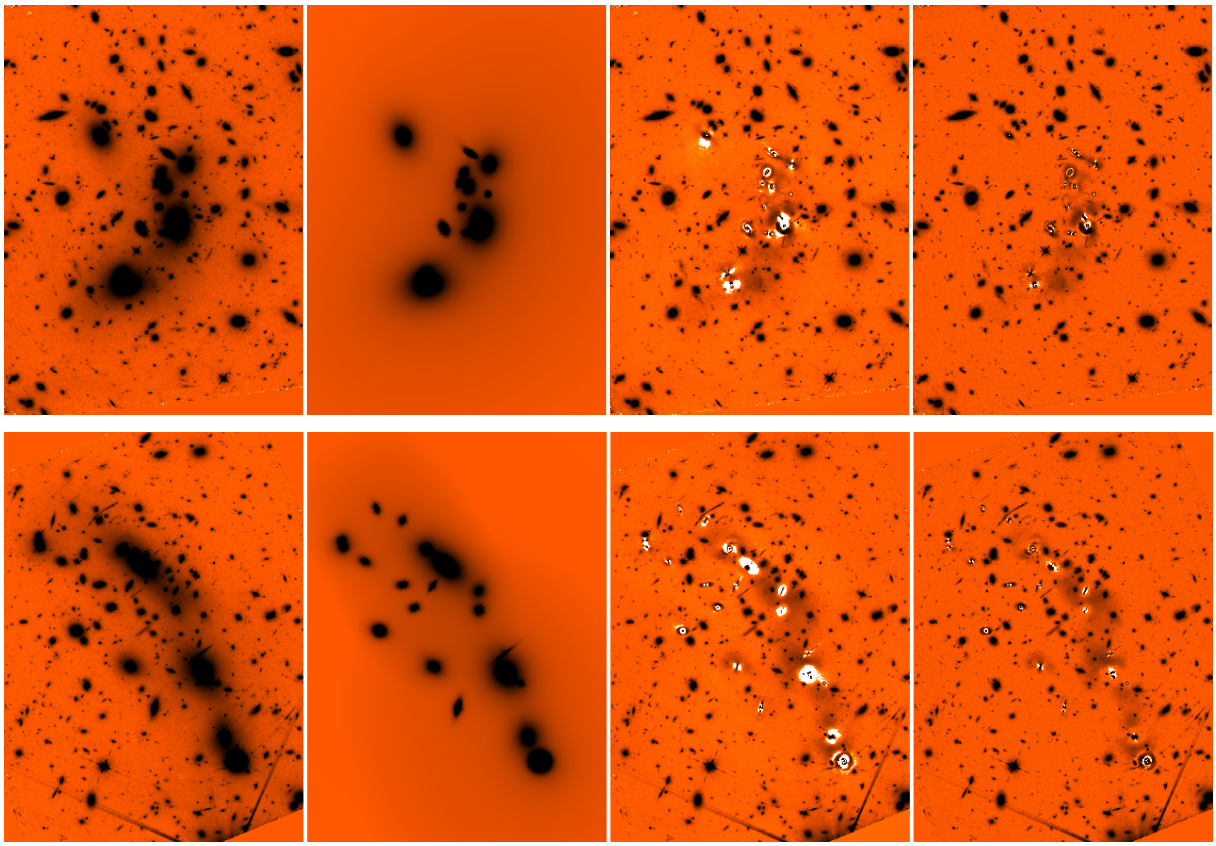

Fig. 2. Effects of the procedure on the A2744 (*top*) and M0416 (*bottom*) $H160$ image. *Left to right*: original image, models of galaxies, and ICL after STEP 4, processed image after subtraction of the models, final processed image after median filtering (STEP 5). All images are in logarithmic greyscale with the same cuts.

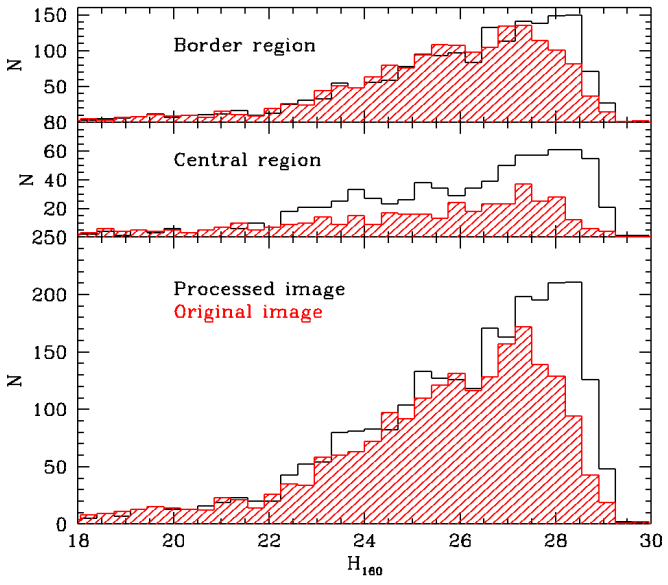

Fig. 3. Detected objects on A2744 cluster field with and without the procedure. *Top*: border region; *middle*: central region; *bottom*: whole field. The central region is defined as a square area centred on the cluster with size 1200 pixels.

In the central regions, we are able to increase the number of detected sources by almost a factor of two, as shown in the middle panel of Fig. 3. Looking at the right panel of Fig. 4, we can see that many detected sources lie close to the removed cluster members. Since it is possible that at least some of them are spurious detections, we flagged them in the final SExtractor catalogue to keep track of potential flaws in the following stages of the process. We choose to flag any detected source having its centroid lying in a region where the normalized flux per pixel of a bright source model is above a given threshold $f_{\rm flag}$. Empirically, we find that taking $f_{\rm flag} = 0.1$ yields reasonable results. See Appendix B for more details on this flag.

4.2. Completeness

We assess detection completeness as a function of the H-band magnitude by running simulations with synthetic sources. Using in-house developed scripts, we first generate populations of point-like (i.e. PSF-shaped) and exponential profile sources, with total H-band magnitude in the range 26.5−30. Disc-like sources are assigned an input half-light radius $R_{\rm h}$ randomly drawn from a uniform distribution between 0.0 and 1.0 arcsec. These fake galaxies are placed at random positions in our detection image, avoiding positions where real sources are observed on the basis of the original SExtractor segmentation map. To avoid an excessive and unphysical crowding of simulated objects, we include 200 objects of the same flux and morphology each time. We then perform the detection on the simulated image, using the same SExtractor parameters adopted in the real case. In Fig. 5, we show the completeness (ratio of the number of recovered to input sources) as a function of the total input magnitude of the simulated objects. We find that the 90% detection completeness for point sources is at $H \sim 27.7$−27.8, and

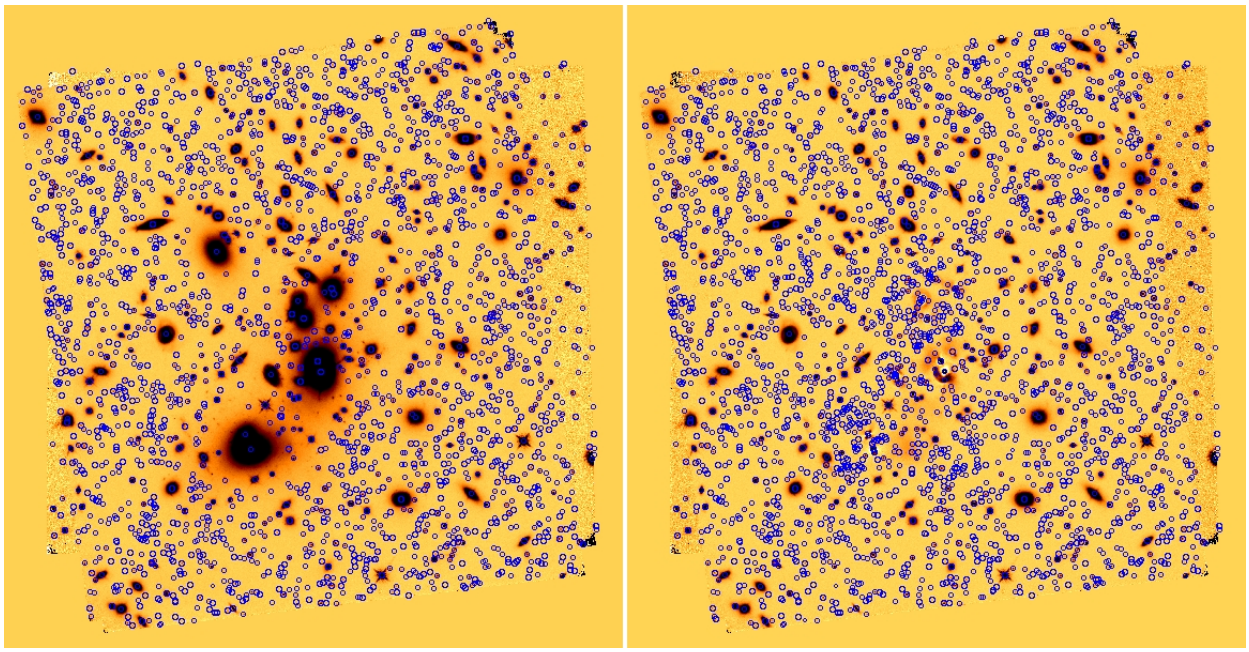

Fig. 4. Detected objects on A2744 cluster field with (*right*) and without (*left*) the procedure.

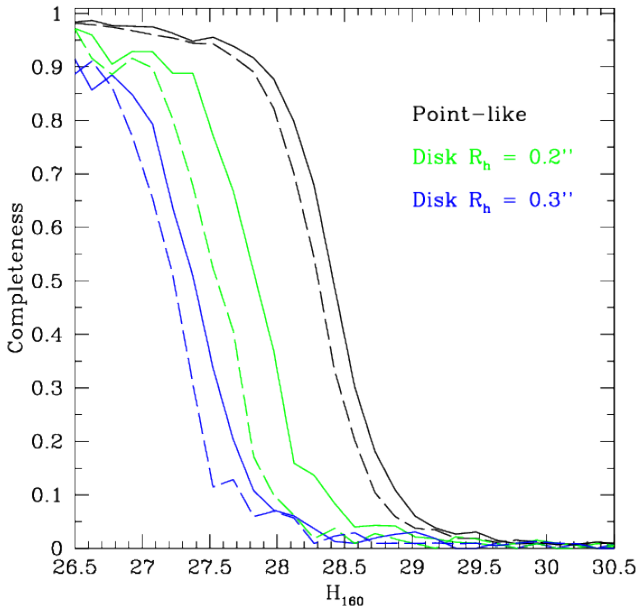

Fig. 5. Detection efficiency (H-detected catalogue) for point-like and disk-like sources in A2744 (continuous lines) and M0416 (dashed lines).

decreases to $H \sim 27.1-27.3$ and $H \sim 26.6-26.7$ for disk-like galaxies of $R_h = 0.2$ arcsec and $R_h = 0.3$ arcsec respectively, the lower values referring to M0416, as expected from its slightly shallower H-band depth.

5. Photometry on the HST images

Having obtained the detection catalogue on the HST H-band images, we proceed to perform the photometric measurements on the other HST bands. To this aim, we process each cluster image to remove foreground sources and ICL, as for the H-band cluster images (again, this is not necessary for the parallel field images). However, having already obtained a robust two component Sérsic fit in the H band, we can now adopt a simpler approach: for each HST image, we use the output from the final GALFIT run on the closest redder band as an input starting guess (e.g. $H160$ output as input for $JH140$, $JH140$ output as input for $J125$, etc.), letting the estimates for positions, magnitudes, radii, and Sérsic indexes free to vary (again applying reasonable constraints on the allowed range of variations: ±3, −1/+5, 1 to 60 and 0.5 to 4.5 for disky components, ±3, −1/+5, 1 to 30, 4.0 to 8.0, and also imposing an axis ratio $q > 0.5$ for the bulgy component). For the ICL, we impose Σ_0 −1/+5, radius 2000 to 5000.

After this procedure, we convolve all the images down to the $H160$ resolution ($FWHM = 0.2''$), with a convolution kernel that was obtained taking the ratio of the PSFs of the two images in the Fourier space. We also apply the median filtering process, described in Sect. 3.5, to all the images, since the simulations showed that the photometric measurements are more robust and the scatter in the measured fluxes is reduced using the median-filtered images.

We then run SEXTRACTOR in dual mode to measure aperture and isophotal photometry.

6. *K* and IRAC photometry

As described in Sect. 2, several independent programs have been obtaining data on the FF regions. In particular, both new deep K and *Spitzer* (3.6 and 4.5 μm) images are available for analysis.

To extract photometric measurements on such lower resolution NIR images, we perform a fit on the images with a PSF-matching technique, by means of the code T-PHOT (Merlin et al. 2015). T-PHOT uses the spatial and morphological information from a high-resolution image as priors to construct low-resolution normalized models, obtained via convolution with a PSF-matching kernel, and simultaneously fits all the objects in the field re-scaling the fluxes of these models. The code enables

real high-resolution cutouts of sources to be used as priors together with analytical models; we took advantage of this option to simultaneously fit the faint sources with the models of the bright cluster members (the latter having the two components stacked to obtain single component models, to avoid possible degeneracy issues in the fitting procedure)[8].

To minimize the effects of too small a segmentation, the SExtractor output map has been "dilated" before being fed to T-PHOT, enlarging the size of the segmented area of each source (the procedure is the same as that adopted for the CANDELS TFIT photometry and is described in Galametz et al. 2013).

6.1. Preparation of the measurement images

We estimate the PSF on the Hawk-I K images, stacking well isolated stellar sources with the same procedure adopted for the HST images. For IRAC, we find that a better approximation can be obtained using a synthetic PSF, constructed using an STScI script described in Galametz et al. (2013), which stacks multiple renditions of the synthetic ideal PSF, each one oriented consistently with the position angle of a single pointing and weighted by the pointing exposure time.

We also correct the rms maps, so that sources at the detection limit have measured fluxes distributed consistently with the statistical expectation. To do this, we randomly select 200 positions in the parallel fields, far enough away from detected sources (this was achieved building a 2σ level mask and taking only the unmasked regions into consideration). Then, we measure the flux of fake point sources injected at the selected positions and compute the rms map multiplicative factor that is required to make the distribution of the measured S/N have a standard deviation that is consistent with 1.

We also further correct the background, measuring the shift of the mean of the distribution of the same fake sources on copies of the images having small constant artificial background offsets, and computing the offset $\Delta_{\rm bkgd}$ required to make the measured shift consistent with zero:

$$\Delta_{\rm bkgd} = \frac{f_- + f_+}{f_- - f_+} \times \Delta_{\rm bkgd,in}, \quad (3)$$

where f_- and f_+ are the mean-measured fluxes of the fake sources in two images having $\pm\Delta_{\rm bkgd,in}$ small constant background offset. We finally assume that the background and rms-correcting factors obtained for the parallel fields are also valid for the clusters fields, since it would be hard to find a sufficient number of void regions in the crowded and relatively small cluster images.

6.2. T-PHOT runs

After preparing the measurement images, we proceed with the T-PHOT runs. For the cluster images we found that simply including the ICL models in the list of sources and fitting them together with all the other priors yields unsatisfactory results. We have therefore developed a different procedure, where we estimate the local background independently for each source, and then combine all these measurements to build a large-scale background image. To this end, we have included in the T-PHOT runs a more complex description of all objects, adding a free parameter to describe the local background. This has been possible without modifying the code, but simply adding an additional analytic component:

- for each source, a "twin" template with the same extension and top-hat flat normalized profile has been coupled to the "true" model template (excluding the bright source models);
- these "background" templates are fitted together with the convolved models of the real cutouts, during the T-PHOT run;
- a model image is produced using only the "background" templates, multiplied by their fitting factors;
- this raw background map is then smoothed with a Gaussian kernel and subtracted from the original LRI.

The resulting images have the major amount of the local background well removed. We finally fit these background-subtracted images again with T-PHOT. Figure 6 shows the original images and the corresponding residual images, obtained subtracting the scaled models generated by T-PHOT. Figure 7 shows the effects of the local background subtraction process in the case of the A2744 Ks image, comparing the residuals from a straightforward T-PHOT run with the residuals obtained with our process.

We follow the same strategy to process the parallel fields (of course without the need to include any analytical model in the priors list).

In all cases, the uncertainties on the measured fluxes are given by T-PHOT as the square root of the diagonal terms in the covariance matrix of the system (see Merlin et al. 2015). Additional information on the reliability of the fit are given by a set of flags in the T-PHOT output. In particular, the covariance index c_i (defined for each source as the ratio between its maximum covariance term and its variance in the covariance matrix) is an important diagnostic that can point out unreliable measurements, helping to identify sources affected by strong contamination from neighbours, potentially causing failures of the measurement method. Figure 8 shows the values of the covariance index as a function of the measured fluxes for the cases of Ks and IRAC 3.6 μm A2744 cluster field. Clearly, many IRAC sources show a high degree of contamination, which can (but not necessarily does) cause problems in the measurement. Sources having $c_i > 1$ should be considered with caution. This diagnostic can be very useful for the correct determination of photometric redshifts and we use it in our analysis (see C16).

7. Additional faint IR-detected sample

Performing the detection in a single band provides clear advantages in terms of a selection function that is more robust and easier to estimate. Our procedure to "clean" the image from bright cluster sources and from the ICL allowed us to turn the FF cluster pointings into "blank" fields, such that our H-band detected catalogue can be considered as complementary to public H-detected catalogues in wider, albeit shallower, areas (e.g. Guo et al. 2013; Galametz et al. 2013). However, the resulting catalogue is not as deep as the one that could be obtained out of a stack of IR images. For instance, a combined Y+J+H detection is, in principle, more effective in selecting blue galaxies at redshifts ∼6−8. For this reason we complement our catalogues with lists of objects detected in a weighted mean of the $Y105$+$J125$+$JH140$+$H160$ bands while undetected in the H-band. This IR-stack is built from the processed GALFIT residual images and used as a detection band in the same way as the $H160$ one. We then individuate all sources whose segmentation does not overlap with any pixel belonging to H-detected sources

[8] We first tried to process the measurement images with the same procedure adopted for the HST images, subtracting the foreground sources to fit only the H-detected objects, but the results were not satisfactory.

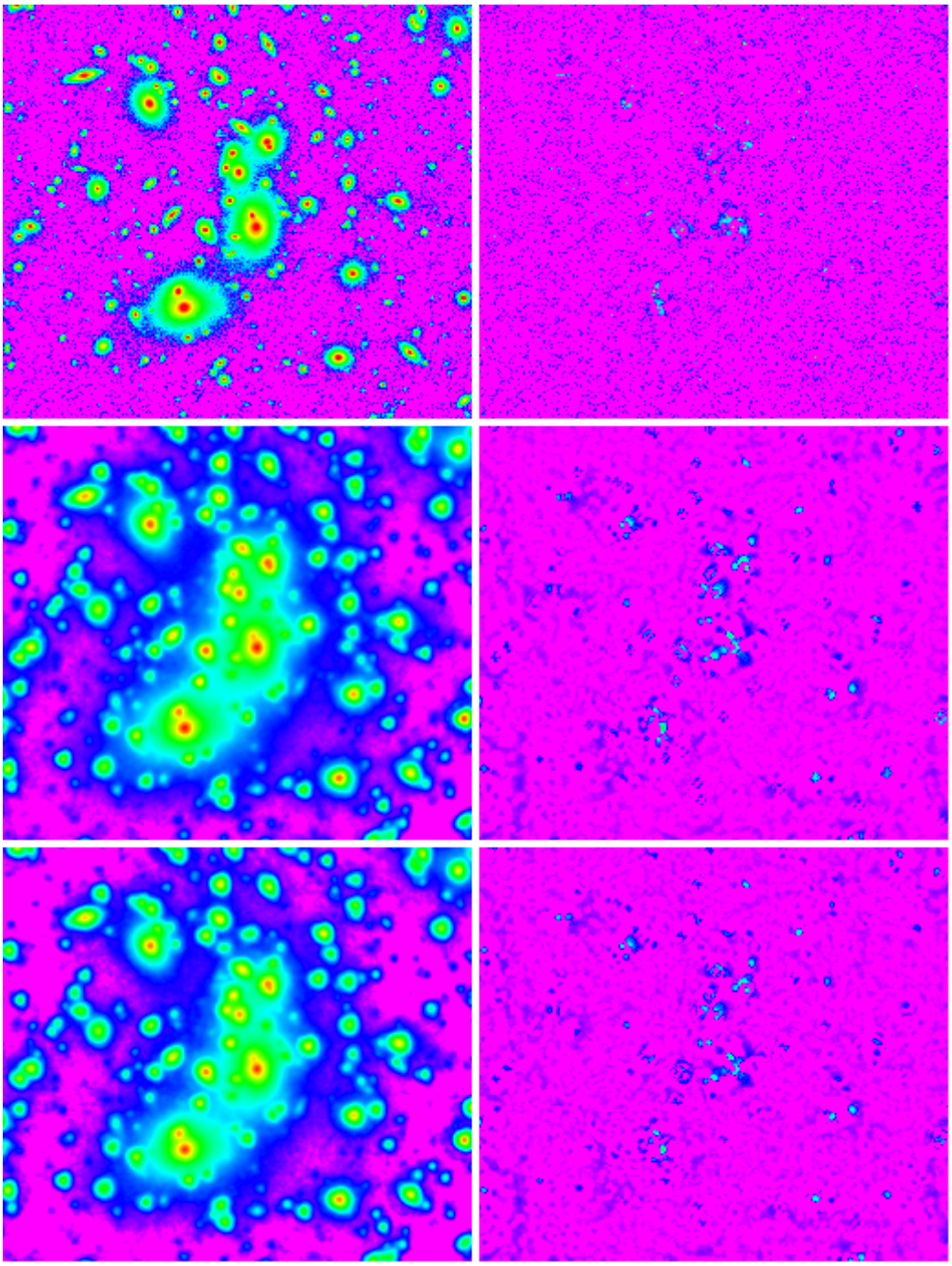

Fig. 6. A2744 residuals after T-PHOT processing. *Left to right*, *top to bottom*: original and residual images of K, IRAC-CH1 and IRAC-CH2, in logarithmic scale.

according to the relevant $H160$ segmentation map. In this way, we isolate 976, 1086, 832, 1152 objects in A2744 cluster, A2744 parallel, M0416 cluster, and M0416 parallel respectively. These are mostly sources with $S/N(\mathrm{H160}) < 5$ and $\mathrm{H160} \sim 27-30$ (Fig. 9).

To assess consistency between the photometry in the H-detected and the IR-detected catalogues, we compare the fluxes of bright sources in common between the two (matched within $0.2''$ radius). We verify that the photometry is consistent with no appreciable offsets both in the HST and in the T-PHOT extracted bands. This test shows that no systematic is introduced in HST and in T-PHOT fluxes by the use of a different detection image, or by a different number of (faint) priors.

8. Diagnostics

As a first check on the reliability of our results, we present some diagnostic checks.

Figure 9 presents the differential number counts for the four considered fields, as a function of the measured $H160$ magnitude. Fluxes are corrected for Galactic extinction, as derived from Schlegel et al. (1998) dust emission maps[9]. We also include the counts from the IR-detected catalogue. The four fields are in good agreement with each other and show an overall

[9] We used the on-line calculator `https://ned.ipac.caltech.edu/forms/calculator.html` to compute the extinction in the passbands of interest, at the central positions of the four fields.

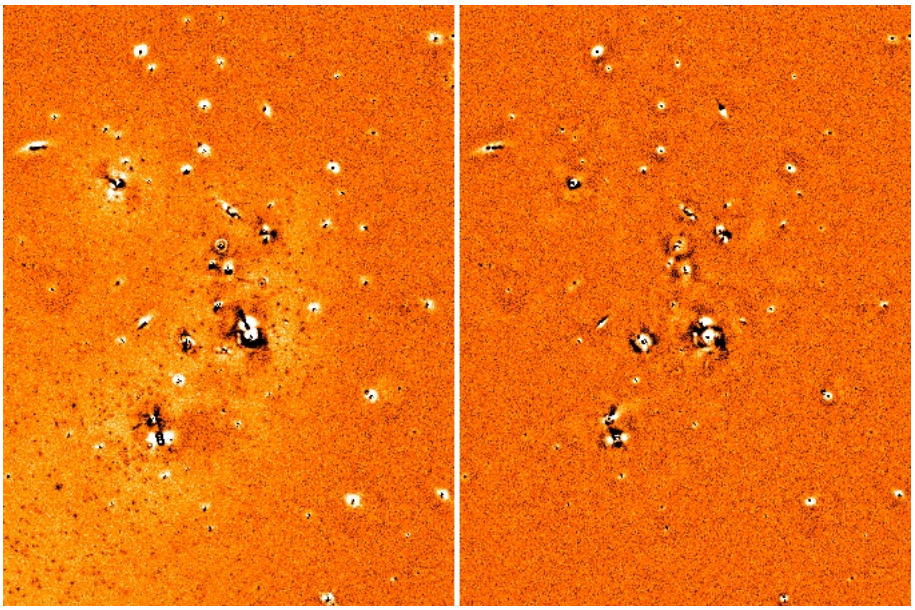

Fig. 7. A2744 *Ks* residuals. *Left*: straightforward T-PHOT run; *right*: with local background subtraction procedure.

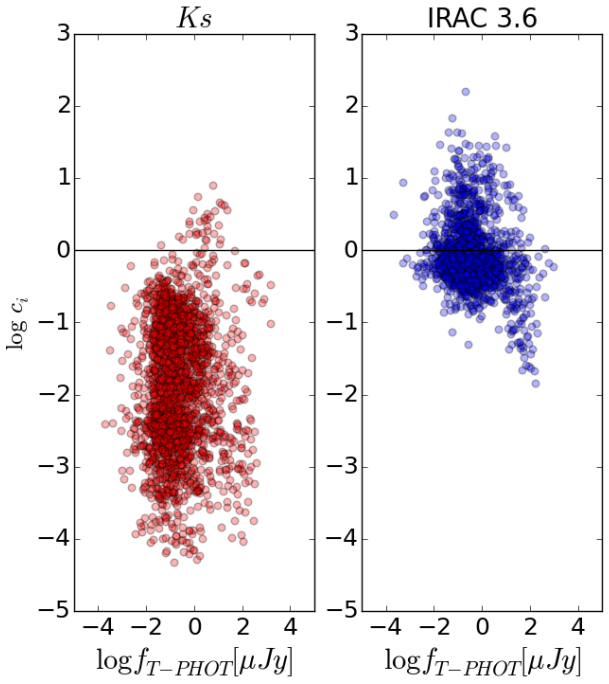

Fig. 8. Covariance index c_i (defined for each source as the ratio between the maximum covariance and the variance) as a function of the measured flux using T-PHOT (shown in $\log \mu$Jy) in the A2744 cluster field. *Left*: *Ks*; *right*: IRAC 3.6 μm. The horizontal line, at $\log c_i = 0.0$, indicates a reference value of reliability for the measured flux. See text for more details.

over-abundance with respect to the number counts on a re-scaled area of the CANDELS fields (GOODS-South and UDS are plotted in the figures, by way of comparison). This effect is perfectly consistent with the expected cluster overdensity and magnification effects (which are also present in the parallel fields, although with relatively lower strength). Indeed, it can be shown that taking into account these effects (removing objects at the clusters redshift and de-magnifying the sources consistently with a cluster mass model) the number counts turn out to be in very good agreement with the CANDELS counts. This is discussed in full detail in C16.

In Fig. 10, three colour−colour plots from the A2744 cluster field (*H*-detected) are shown; the other three fields have similar behaviour. The FF sources are distributed in overall good agreement with the CANDELS objects, with the noticeable exception of a sequence of colour-clustered objects in each of the plots. From the photometric redshift analysis performed in C16, these sources mainly turn out to be cluster members.

Figure 11 presents the fitted spectral energy distribution (SED) of three models of bright A2744 cluster objects (the SED fittings are obtained using the Fontana's photo-z code developed at OAR, see C16 for all the details). The fluxes are obtained with GALFIT for the HST bands, and with T-PHOT for the *Ks* and IRAC bands. Figure 12, on the other hand, shows the fitted SEDs of four objects that have confirmed spectroscopic redshift (Owers et al. 2011; Johnson et al. 2014). In this case the fluxes are obtained with the SEXTRACTOR PSF-matched photometric measurements, for the HST bands, and with T-PHOT, for the *Ks* and IRAC bands. All the fits are quite accurate, showing that the applied recipes are efficient in retrieving reasonable fluxes over the whole range of considered wavelengths.

Finally, Fig. 13 shows a tentative colour selection of high-redshift candidates based on our photometry. Following Atek et al. (2015), the left panel shows the *IYJ* diagram where we search for $z \sim 7$ sources by means of the following selection (we only consider objects that are not flagged as a potentially spurious detection resulting from the foreground light subtraction procedure, see Sect. 4.1):

- no detection in B_{435} and V_{606};
- $(I_{814} - Y_{105}) > 0.8$;
- $(I_{814} - Y_{105}) > 0.6 + 2 \times (Y_{105} - J_{125})$;
- $(Y_{105} - J_{125}) < 0.8$.

The right panel shows the *YJH* diagram where we search for $z \sim 8$ objects by means of the following selection:

- no "residual flag" (see Sect. 4.1);
- no detection in B_{435}, V_{606} and I_{814};
- $(Y_{105} - J_{125}) > 0.5$;
- $(Y_{105} - J_{125}) > 0.4 + 1.6 \times (J_{125} - H_{140})$;
- $(J_{125} - H_{140}) < 0.5$.

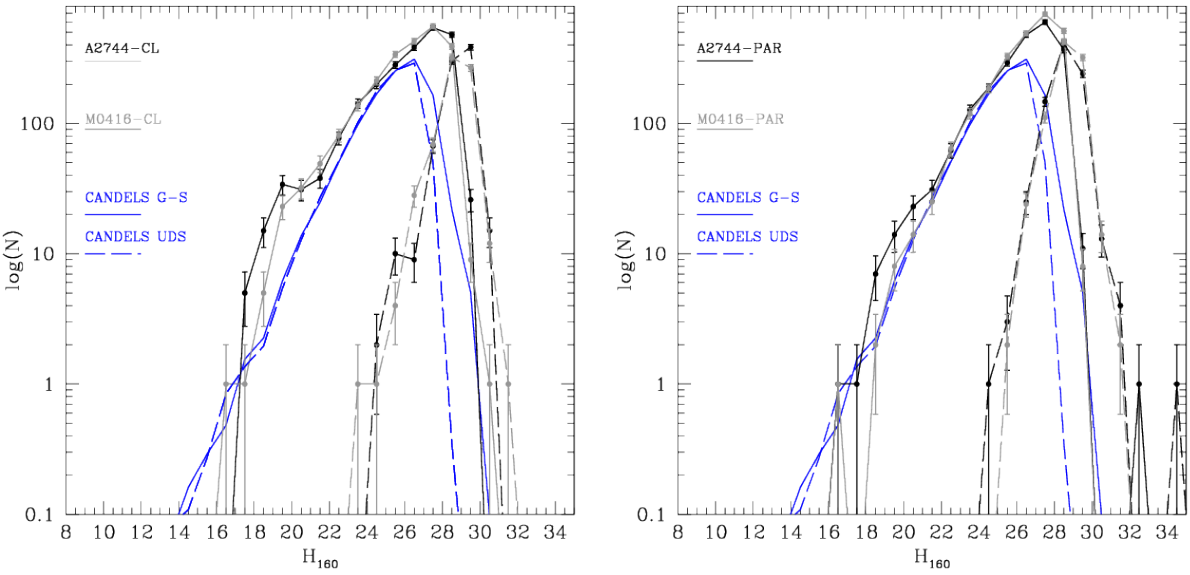

Fig. 9. Raw number counts of detected objects in the detection images. *Top panel*: A2744; *bottom panel*: M0416. Black lines refer to the cluster fields, blue lines to the parallel fields; solid lines refer to the *H*-detected catalogue; dashed lines: the additional IR-stack detected catalogue. For reference, the red lines refer to CANDELS fields number counts re-scaled to the FF area (solid: GOODS-South, dashed: UDS). See text for details.

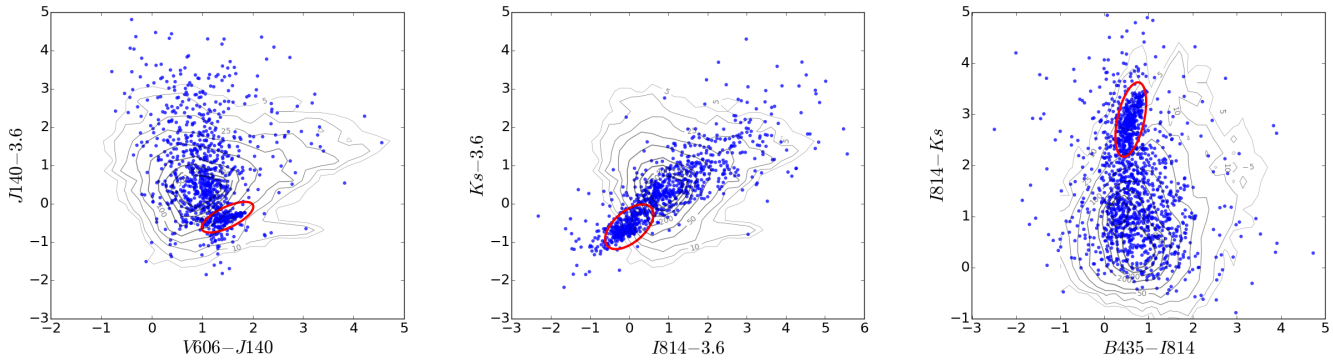

Fig. 10. Colour–colour diagrams. Grey lines are number density contours for GOODS-South CANDELS objects, using Guo et al. (2013) photometry. Blue dots: A2744 cluster field, this work (only objects detected in all relevant bands are included). The large majority of the objects inside the red ellipses, which deviate from the typical distributions, are likely to be cluster members, as confirmed by the photo-z analysis in C16.

We compare our results with those from the similar selection by Atek et al. (2015, their high-redshift candidates are marked with large open circles in the two colour−colour diagrams, after a process of spatial cross-correlation between the two catalogs). We find an overall good agreement between the two sample selections, in both redshift intervals, with the noticeable exceptions of eight sources (out of 29) in the $z \sim 7$ diagram, which fall shortly outside of the selection region when using our photometry. In C16, a comparison between the photometric redshifts derived from our photometry and other redshift estimates found in the literature is presented and discussed, finding a very good agreement for high-z sources including those in the Atek et al. (2015) sample. On the other hand, we identify a number of new candidates, many of which (particularly in the $z \sim 8$ selection) are *IR*-detected sources. In total, with this method we find 107 $z \sim 7$ candidates (85 of which are *IR*-detected) and 31 $z \sim 8$ candidates (28 of which are *IR*-detected). At a visual inspection, all these objects appear as reasonable high-redshift candidates. A thorough analysis of the topic is beyond the scope of this paper, and we leave it for future studies; however, this basic sanity check helps to strengthen the reliability of our photometry.

9. Summary and conclusions

We have presented the complete multiwavelength photometric catalogues of the first two publicly released FF datasets, Abell-2744 and MACS-J0416, along with the methodology we adopted to obtain them. The catalogues cover four fields: the two clusters fields and the two corresponding parallel fields. In each catalogue, we list the total fluxes of the *H*-band and IR-stack detected sources, in ten passbands: HST ACS *B*435, *V*606, *I*814; HST WFC3 *Y*105, *J*125, *JH*140 and *H*160; VLT Hawk-I *Ks* 2.146 μm (ground-based); and *Spitzer* IRAC 3.6 and 4.5 μm. To detect faint objects that are outshone by bright foreground sources and the ICL in the two cluster fields, we developed a procedure to remove the light coming from these sources in

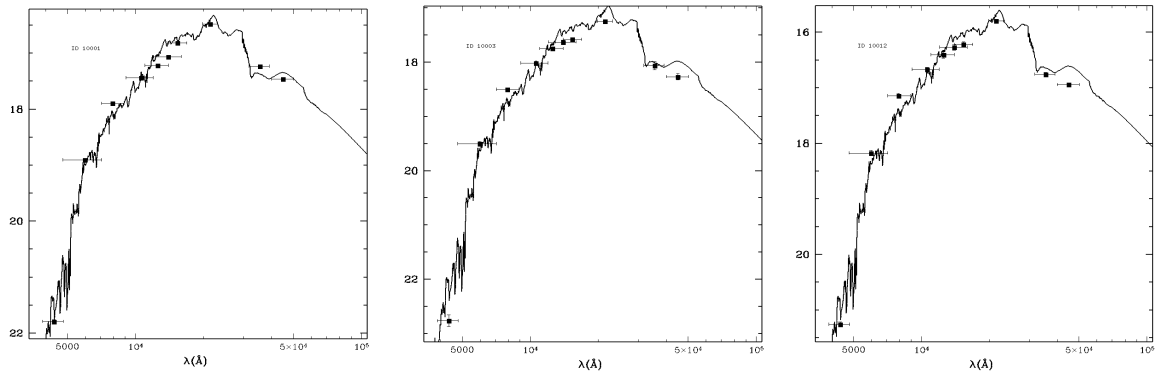

Fig. 11. Examples of SED fitting with photometry from this work, for three models of bright cluster sources belonging to A2744 (z = 0.308).

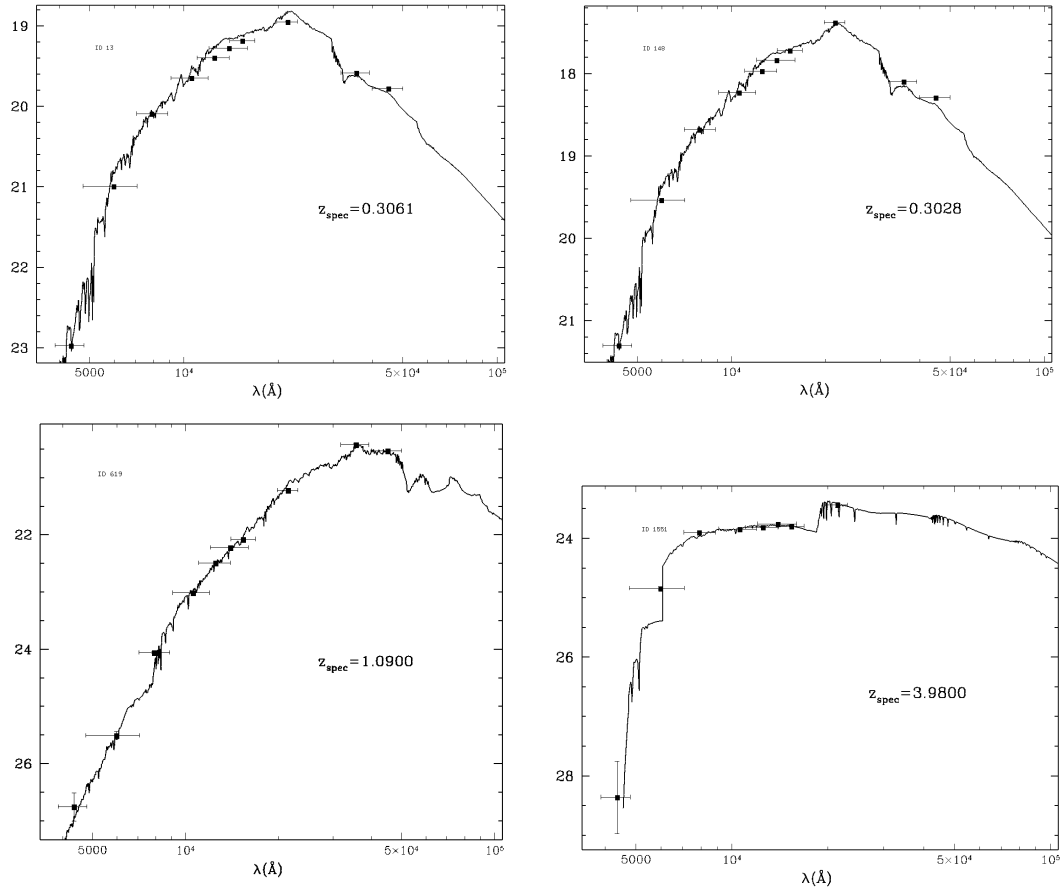

Fig. 12. Examples of SED fitting with photometry from this work, for four objects with known confirmed spectroscopic redshift in the A2744 cluster field.

the detection image (H-band or IR-stack), fitting their light profiles with analytical models by means of the two public codes GALAPAGOS and GALFIT, applying a median filtering to the processed images, and using SEXTRACTOR with a HOT+COLD approach. The parallel fields are processed with a more straightforward approach, directly running SEXTRACTOR on the H-band image.

The photometry in the HST bands is obtained using the SEXTRACTOR dual-mode option on PSF-matched images (convolved down to the H-band resolution). All HST cluster images are also processed as the detection image, removing the light from bright foreground sources. K and IRAC fluxes are measured with T-PHOT, including an ad hoc option to subtract local background light. In the case of the cluster fields, real sources and analytical models of bright objects are fitted simultaneously.

The catalogues also report the uncertainties on the flux measurements, as computed by means of the different techniques adopted to measure the fluxes, as well as some additional diagnostic information (flags).

The first scientific applications of the catalogues, including photometric redshifts, magnification, and physical properties, are presented in the companion paper by Castellano et al. (2016).

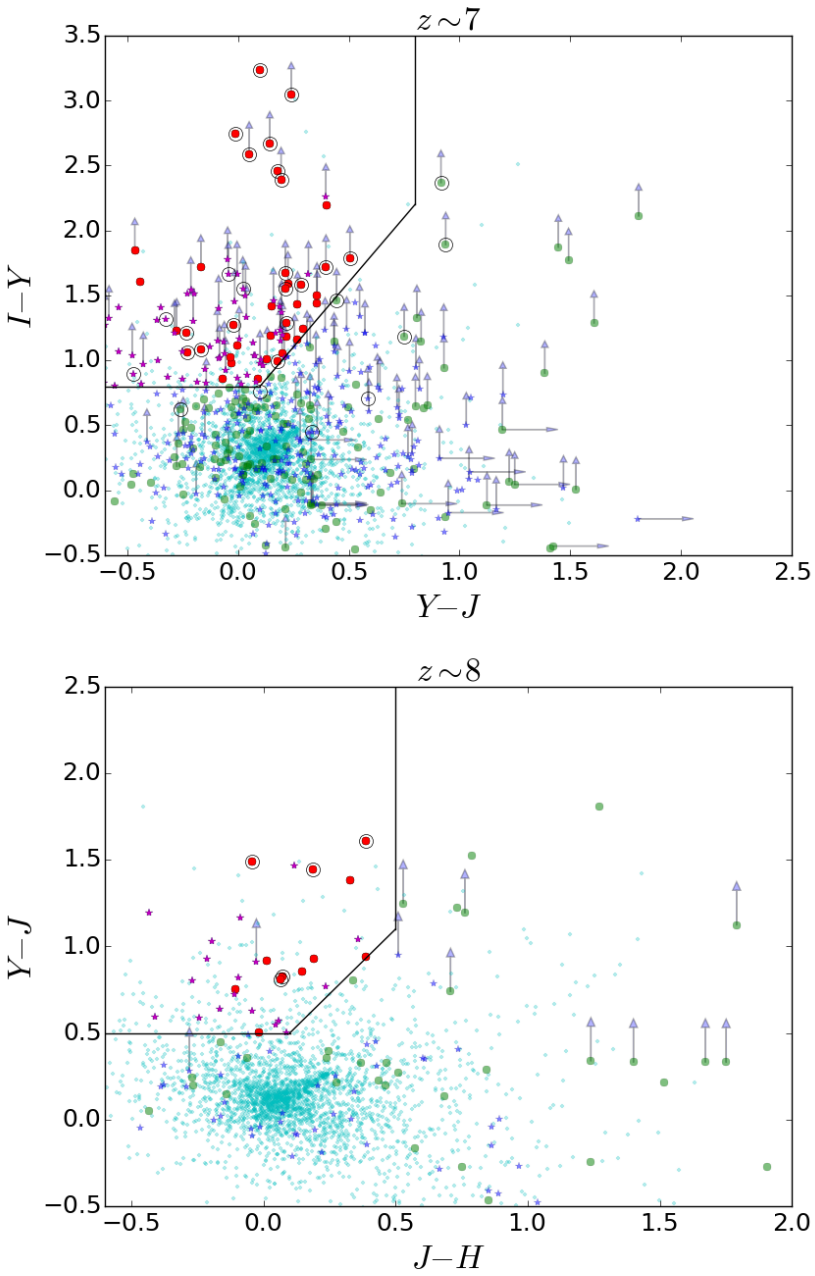

Fig. 13. Colour selection of high-redshift sources. *Top panel*: *IYJ* diagram for $z \sim 7$ candidates (cyan points: sources with 1σ detection in B_{435} or V_{606}, which we exclude from the selection; green dots: *H*-detected sources, undetected in B_{435} and V_{606}; blue stars: *IR*-detected sources, undetected in B_{435} and V_{606}; red dots: *H*-detected $z \sim 7$ candidates; magenta stars: *IR*-detected $z \sim 7$ candidates; empty black circles: Atek et al. (2015) $z \sim 7$ candidates; arrows represent upper limits). *Bottom panel*: *YJH* diagram for $z \sim 8$ candidates (symbols have the same meaning as in the top panel, except that the cyan points represent sources that we exclude from the selection because they are detected in B_{435}, in V_{606}, or in I_{814}).

Acknowledgements. The research leading to these results has received funding from the European Union Seventh Framework Programme (FP7/2007-2013) under grant agreement No. 312725. J.S.D. acknowledges the support of the European Research Council via the award of an advanced grant. F.B. acknowledges support by FCT via the postdoctoral fellowship SFRH/BPD/103958/2014 and also the funding from the programme UID/FIS/04434/2013.

References

Agüeros, M. A., Ivezić, Ž., Covey, K. R., et al. 2005, AJ, 130, 1022
Atek, H., Richard, J., Kneib, J.-P., et al. 2015, ApJ, 800, 18
Barden, M., Häußler, B., Peng, C. Y., McIntosh, D. H., & Guo, Y. 2012, MNRAS, 422, 449
Bertin, E., Mellier, Y., Radovich, M., et al. 2002, in Astronomical Data Analysis Software and Systems XI, eds. D. A. Bohlender, D. Durand, & T. H. Handley, ASP Conf. Ser., 281, 228
Binney, J., & Tremaine, S. 1987, Galactic dynamics (Princeton: NJ Princeton University Press)
Castellano, M., Amorín, R., Merlin, E., et al. 2016, A&A, 590, A31
Galametz, A., Grazian, A., Fontana, A., et al. 2013, ApJS, 206, 10
Giallongo, E., Menci, N., Grazian, A., et al. 2014, ApJ, 781, 24
Grogin, N. A., Kocevski, D. D., Faber, S. M., et al. 2011, ApJS, 197, 35
Guo, Y., Ferguson, H. C., Giavalisco, M., et al. 2013, ApJS, 207, 24
Johnson, T. L., Sharon, K., Bayliss, M. B., et al. 2014, ApJ, 797, 48
Koekemoer, A. M., Avila, R. J., Hammer, D., et al. 2014, AAS, 223, 254.02
Laporte, N., Streblyanska, A., Kim, S., et al. 2015, A&A, 575, A92
Lotz, J., Mountain, M., Grogin, N. A., et al. 2014, in AAS Meeting, 223, 254.01
McLeod, D. J., McLure, R. J., Dunlop, J. S., et al. 2015, MNRAS, 450, 3032
Merlin, E., Fontana, A., Ferguson, H. C., et al. 2015, A&A, 582, A15
Obrić, M., Ivezić, Ž., Best, P. N., et al. 2006, MNRAS, 370, 1677
Oesch, P. A., Bouwens, R. J., Illingworth, G. D., et al. 2015, ApJ, 808, 104
Owers, M. S., Randall, S. W., Nulsen, P. E. J., et al. 2011, ApJ, 728, 27
Schlegel, D. J., Finkbeiner, D. P., & Davis, M. 1998, ApJ, 500, 525
Sérsic, J. L. 1968, Atlas de galaxias australes (Cordoba, Argentina: Observatorio Astronomico)
Wang, X., Hoag, A., Huang, K.-H., et al. 2015, ApJ, 811, 29

Table A.1. SExtractor COLD and HOT mode parameter sets.

Parameter	COLD	HOT
DETECT_MINAREA	10.0	6.0
DETECT_THRESH	0.7	0.82
ANALYSIS_THRESH	0.7	0.82
DEBLEND_NTHRESH	64	64
DEBLEND_MINCOUNT	0.0001	0.0001
BACK_SIZE	128	32
BACK_FILTERSIZE	1	3
BACKPHOTO_TYPE	local	local
BACKPHOTO_THICK	48.0	48.0
MEMORY_OBJSTACK	400	400
MEMORY_PIXSTACK	4 000 000	4 000 000
MEMORY_BUFSIZE	500	500

Notes. A Gaussian filtering (*FWHM* = 4.0 pixels) was applied for the detection runs.

Appendix A: SExtractor parameters for detection

Table A.1 lists the parameters adopted in the SExtractor detection runs described in Sect. 4.1.

Appendix B: Catalogue formats

In all the catalogues, the IDs are organized as follows:

- *H*-detected objects have IDs starting from 1;
- IR-detected objects have IDs starting from 20 000;
- the bright cluster objects, modelled and subtracted from the HST images, have IDs starting with 100 000.

The formats of the released catalogues are as follows:

- *Catalogue A – magnitudes*: in the first catalogue we list IDs, position, AB magnitudes, and relative uncertainties in the ten bands under consideration. The format is therefore
  `ID RA DEC X Y MAG_B435 MAG_V606 MAG_I814 MAG_Y105 MAG_J125 MAG_JH140 MAG_H160 MAG_Ks MAG_IRAC1 MAG_IRAC2 MAGERR_B435 MAGERR_V606 MAGERR_I814 MAGERR_Y105 MAGERR_J125 MAGERR_JH140 MAGERR_H160 MAGERR_Ks MAGERR_IRAC1 MAGERR_IRAC2`.
- *Catalogue B – fluxes*: a second catalogue contains IDs, fluxes, and uncertainties of the fluxes (μJy). The format is
  `ID FLUX_B435 FLUX_V606 FLUX_I814 FLUX_Y105 FLUX_J125 FLUX_JH140 FLUX_H160 FLUX_Ks FLUX_IRAC1 FLUX_IRAC2 FLUXERR_B435 FLUXERR_V606 FLUXERR_I814 FLUXERR_Y105 FLUXERR_J125 FLUXERR_JH140 FLUXERR_H160 FLUXERR_Ks FLUXERR_IRAC1 FLUXERR_IRAC2`.
- *Catalogue C – diagnostics*: a third catalogue contains useful diagnostic data. It lists IDs, position in *H*160 image pixel reference, segmentation limits, SExtractor CLASS_STAR parameter, the flag we applied to residual features after processing the detection image (see Sect. 4.1), a "visual inspection flag" to select spurious detections, the flag given by T-PHOT to identify saturated and blended priors, and the information on the covariance of the sources (ratio of maximum covariance to the variance) for the *K*s and IRAC bands. The format is
  `ID X Y XMIN YMIN XMAX YMAX CLASS_STAR SEXFLAG RESFLAG VISFLAG TPHOTFLAG_Ks COVMAX_Ks TPHOTFLAG_IRAC1 COVMAX_IRAC1 TPHOTFLAG_IRAC2 COVMAX_IRAC2]`.